

Modeling 65 Years of Land Subsidence in California's San Joaquin Valley

Matthew Lees (✉ mlees0209@gmail.com)

Stanford University <https://orcid.org/0000-0003-1717-515X>

Rosemary Knight

Stanford University

Ryan Smith

Missouri University of Science and Technology

Physical Sciences - Article

Keywords: Modeling, 65, Years, Land Subsidence, California, San Joaquin Valley

Posted Date: June 11th, 2021

DOI: <https://doi.org/10.21203/rs.3.rs-609832/v1>

License: © ⓘ This work is licensed under a Creative Commons Attribution 4.0 International License.

[Read Full License](#)

Modeling 65 Years of Land Subsidence in California's San Joaquin Valley

Matthew Lees^{a*}, Rosemary Knight^a, Ryan Smith^b

a) Stanford University, Stanford, CA, USA; b) Missouri University of Science and Technology, Rolla, MO, USA

* Corresponding author; mlees0209@gmail.com

Land subsidence, caused by groundwater extraction and subsequent subsurface compaction, is an issue of global concern^{1,2}. Since the 1920s, there have been numerous periods of subsidence in California's San Joaquin Valley leading to widespread sinking of the land surface which has locally exceeded 9 m³⁻⁵. The most recent period of severe subsidence, which was triggered by the 2012-15 drought, is now causing damage which threatens the long-term viability of critical water distribution infrastructure in the Valley^{6,7}. However, there is neither a continuous monitoring record of the subsidence nor high-quality records of the hydrologic head changes in the subsurface which have caused the subsidence, making it impossible to understand, and thus mitigate, the subsidence. Here, we leverage subsidence and hydraulic head data from a variety of sources to create and validate a one-dimensional model of subsurface compaction and subsidence over the 65 years between 1952-2017. This model, which simulated up to 7.5 m of subsidence since 1952, provides a complete record of subsidence in our study region by filling crucial gaps in the observed record. Our model reveals the long-term processes causing subsidence, which operated over decades-to-centuries and caused exceptionally high rates of baseline subsidence in 2017, resulting in a critical risk of future subsidence. This risk is exacerbated as the Valley moves into drought conditions again in Spring 2021⁸. We demonstrated an approach which provided the understanding of subsidence in the Valley needed to directly inform sustainable groundwater management, and which is applicable in subsiding regions around the World.

Main text

In California's San Joaquin Valley, land subsidence has been a recurring problem since the 1920s⁹⁻¹¹. Similar to many sedimentary aquifer systems worldwide, the major source of subsidence in the San Joaquin Valley is the compaction of subsurface clays in response to groundwater extraction^{12,13}. Between the mid-1920s and early-1970s, a period of extreme subsidence occurred in the Valley, resulting in a maximum observed subsidence exceeding 9 m³ and millions of dollars of damage to wells, water-conveyance structures and other infrastructure^{14,15}. During this period, a comprehensive monitoring program was established under the leadership of Joseph Poland of the U.S. Geological Survey, including regular levelling surveys and a network of extensometers which measured the compaction at different depths in the aquifer system¹⁶. By 1970, increased availability of surface water greatly reduced groundwater extraction, and subsidence rates diminished to near-zero by 1980³; the monitoring program was largely abandoned in the decades that followed¹⁷. However, some limited subsidence was again observed during both the 1976-77 and 1987-92 droughts^{3,17}. Far worse occurred during two periods of severe drought in 2007-10 and 2012-15, when subsidence returned at rates comparable to those observed in the 1920s-1970s⁵, triggering damage to canals, bridges and other infrastructure^{18,19}. This recent subsidence, along with other negative environmental impacts of excessive groundwater extraction, led to the passage of a groundbreaking piece of legislation in 2014 - the Sustainable Groundwater Management Act (SGMA), which requires groundwater managers to take action to reduce future significant

subsidence. The passage of SGMA, along with renewed drought conditions in the San Joaquin Valley in Spring 2021, makes understanding the controls on subsidence in the Valley a critical and urgent issue.

While our understanding of the recent subsidence has been hindered by the absence of a comprehensive monitoring network like that of the Poland era, we now have available geodetic data from Interferometric Synthetic Aperture Radar (InSAR) satellites. InSAR has been applied to create maps displaying subsidence in the San Joaquin Valley during several time windows between 2002 and present²⁰⁻²³; the resulting images of the sinking of land in the Valley are a compelling reminder of the urgent need for sustainable groundwater management. However, InSAR observations have two significant limitations: 1) they provide measurements of total subsidence but contain no direct information about the specific depth intervals over which compaction is occurring and 2) they leave us without detailed information about subsidence outside of the relatively short periods for which high-quality data are available, which are the 2007-10 and 2015-present time periods²⁴.

The first limitation is particularly important given the multi-layered aquifer system of the San Joaquin Valley. At most locations, it is comprised of an upper and lower aquifer separated by the regional confining unit known as the Corcoran Clay. While extensometer data gathered in the Poland-era showed that compaction primarily occurred in the lower aquifer^{3,9}, the extensometer network was abandoned in the 1980s and there are almost no extensometers active in the areas affected by recent subsidence (Figure S 2). As a result, we have no direct monitoring of the depth at which compaction occurs, which is a key consideration in understanding the controlling mechanisms.

The second limitation has reduced our ability to assess the long-term features in the subsidence record and determine how groundwater extraction in the past has contributed to the recent subsidence. Modeling during the Poland era predicted decades to centuries of so-called deferred subsidence, which is subsidence that occurs due to past, but not current, groundwater extraction^{3,25}. However, several recent InSAR-based studies have described deferred subsidence as lasting for only one-to-two years after the 2007-10 and 2012-15 droughts^{24,26,27}. This discrepancy likely stems from the short monitoring period provided by the InSAR satellites, rather than a change in the nature of the compaction.

A powerful approach to address these gaps in monitoring and understanding is to use physical models to simulate the subsurface compaction which causes the subsidence. The aquitard-drainage conceptual model, developed during the Poland era²⁸, remains our best theoretical description of how groundwater pumping triggers compaction and therefore subsidence. It describes how water pumped from the parts of the aquifer system dominated by coarse-grained materials (sand and gravel) causes a drop in the hydraulic head and corresponding increase in grain-to-grain stresses in those parts of the aquifer system. These increased stresses only cause limited compaction due to the low compressibility of sand and gravel. Over time, however, the hydraulic head drop spreads into adjacent clay interbeds and aquitards, triggering large compaction rates in those highly compressible parts of the aquifer system. This compaction is responsible for the majority of observed subsidence. The timescale over which a head drop propagates from the sands and gravels into a clay layer is related to the clay's hydraulic

properties and thickness, and is typically large. This is the cause of deferred subsidence. In this study, our approach was to use a one-dimensional numerical implementation of the aquitard drainage model to simulate subsidence, in order to fill the observational gaps and improve our fundamental understanding of subsidence in the San Joaquin Valley.

Our modelling focused on a small study region just south of the town of Hanford (Figure S 1). The major breakthrough that launched our modelling effort was the creation of the 65-year head timeseries from 1952-2017 in the coarse-dominated material for both the upper and lower aquifers. To make these timeseries, we analyzed and combined head data from eight different wells within the study region, a procedure which is fully described in *Methods 1*. The remaining model inputs, and the model equations, are described in *Methods 2-6*. Where uncertainty was identified in input parameters, our approach was to use a grid-search through all possible inputs and validate the model output with observed subsidence data. We validated against observed subsidence data from two InSAR datasets (2007-10 and 2015-17) and from two levelling surveys (1966-70 and 1960s-2004), which provided excellent constraint on both short and long-term subsidence rates. Out of a grid search of over 6000 parameter combinations, 27 model runs agreed with the validation data and were retained; these runs provided our modelled subsidence record. Equipped with this record, we were then able to make important insights into the origin of subsidence in the Valley.

A 65-year record of subsidence history

Our model provides a complete history of subsidence rates over the past 65 years, without the substantial gaps of the observational record. We present the 65-year modelled subsidence record, together with the hydraulic head series used as model input, in Figure 1. The information in the middle panel, which shows the available subsidence data, reveals the temporal gaps which we have filled with our model. We are able to clearly discern a recurring pattern over the past 65 years: cycles of head decline in one or both aquifers, accompanied by elevated subsidence rates, followed by periods when the head was stable or undergoing partial recovery and the subsidence continued but at a decreased rate. These cycles can be linked to known hydrologic events that caused the head variations, shown by the shading in Figure 1.

The first cycle started with head decline caused by high groundwater extraction in the 1940s and 1950s^{29,30}, which led to high subsidence rates between 10-30 cm/yr in the 1950s and early 1960s. As surface water supplies became available in the 1970s and 1980s⁹, head levels recovered and subsidence rates fell to 1 cm/yr by 1987. The second cycle began with the 1987-92 drought, where head declined again and subsidence rates increased to 15 cm/yr. After the drought, head recovered and subsidence rates fell again to 3 cm/yr by 1999.

There were three, rapid cycles in the 2000s. The first began in 2001-04, where we observe head declines in both aquifers. This period was not a hydrologic drought: the likely reason for the head declines in this period was a combination of moderately-dry conditions³¹ and a reduction in deliveries of surface water to this area³². These head declines led to a spike in subsidence rates, reaching 15 cm/yr in 2004. Head then recovered until the next cycle which started with the 2007-09 drought, during which we simulated subsidence rates peaking at 17 cm/yr in 2009, and which finished with two years of stable head and reduced subsidence rates from 2010-2012. The final

cycle began with the 2012-15 drought, which caused further, substantial head declines and the greatest simulated subsidence rate of the 65-year modelled period: 37 cm/yr in 2015. In the final two years of our modelled record, 2015-17, head recovered, primarily in the lower aquifer, and subsidence rates fell to 14 cm/yr in 2017. Note that since this 2017 subsidence rate was due entirely to past head drops, it was therefore deferred subsidence. Our model provides the first picture of the subsidence cycles over the past 65 years, including identification of high subsidence rates in the 1987-92 and 2001-04 periods of head decline for which there were no subsidence data in our study region. This 65-year record provides the historic context required to understand the controls on subsidence.

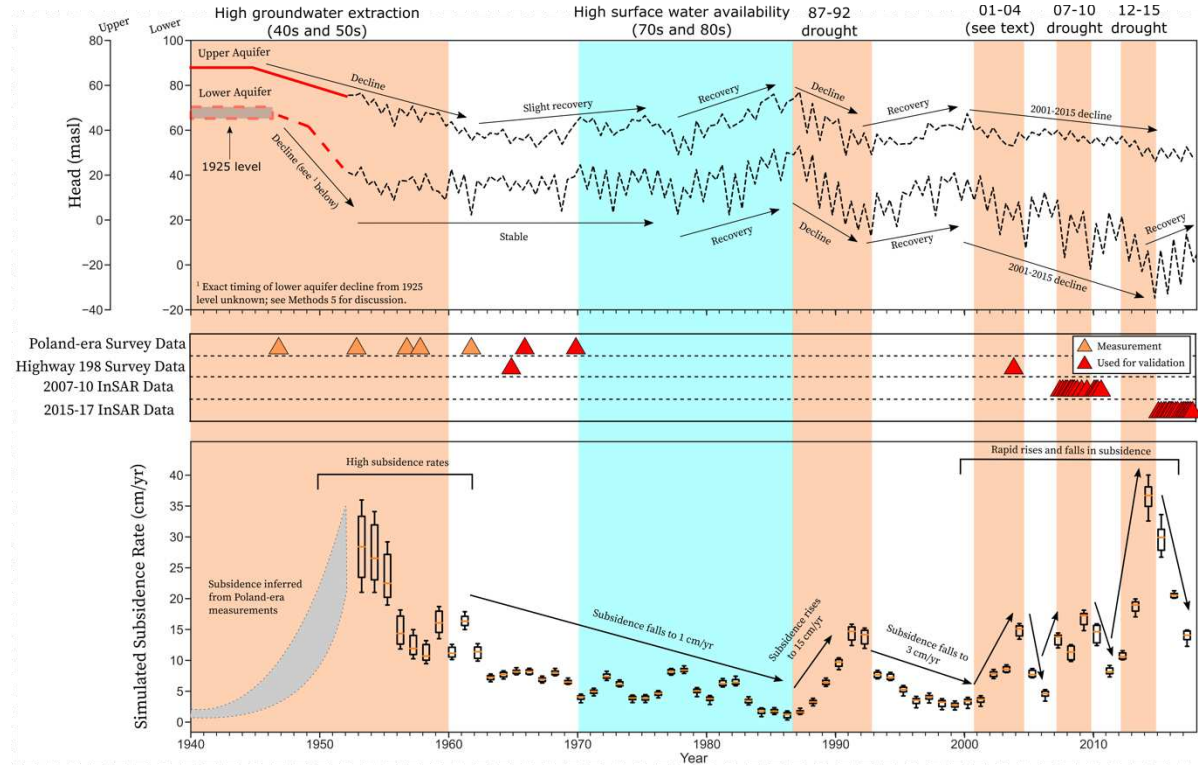


Figure 1 The relationship between hydrologic events, head decline and simulated and observed subsidence. Top: model input head time series, shown with the black dashed lines, for the upper and lower aquifers. Red lines pre-1952 show the approximated head trajectory prior to the model start date; for more information on this, see Methods 5. Middle: observational subsidence data during the modelled period; data points shown in red were used in model validation. Bottom: Subsidence rates from the 27 model runs, shown as a box-and-whisker representation for each water year from 1952-2017. The whiskers represent the 5th and 95th percentiles and boxes show the interquartile range. The median simulated value for each year is represented with a horizontal orange line. Pre-1952 subsidence, shown in the grey arc, was inferred from Poland-era measurements reported in Poland et al. (1975)⁹ and the Inter-agency Committee on Land Subsidence in the San Joaquin Valley (1958)¹⁶. Hydrologic events which caused the head variations are labelled at the top of the figure, and are marked with light orange (head decline) and cyan (head recovery) shading.

Compaction occurs over long timescales

The modelling that we have conducted provides valuable insight into the timescale over which compaction occurs following groundwater extraction. The concept of compaction extending over long timescales, as the head decline propagates into the clay interbeds and aquitards, is widely accepted. However, it is impossible to quantify those timescales without a sufficiently long temporal record of hydraulic head and subsidence. The aquitard-drainage model allows us to calculate an effective time constant (τ) which describes the characteristic timescale over which

head propagation, and hence compaction, occurs (described in *Methods 8*). We tabulated these effective time constants for all 6000+ simulations in our grid search, which gave a range of values from 6 to 2500 years. However, for the 27 simulations which fitted the validation data, the range of time constants contracted to between 60 and 1300 years, which is comparable to those derived from the aquitard-drainage model in the Poland-era²⁵. We note that the shortest value that we obtained, of 60 years, is far larger than the one-to-two year timescales mentioned in recent studies based on short periods of subsidence and head data^{24,26,27,33}. We believe our longer timescales provide an accurate description of the duration of compaction, which was underestimated in recent studies due the limited length of the observational record. Since thick clay aquitards and interbeds are widespread in the San Joaquin Valley, we conclude that timescales on the order of decades to centuries are required to characterize compaction throughout the Valley.

An important implication of the long timescales of compaction is deferred subsidence. The deferred subsidence rate in 2017 was 14 cm/yr, which is as large as peak subsidence rates in the 1987-92 and 2001-04 periods of head decline. Our simulations allowed us to quantify the link between this large deferred subsidence rate and the multiple cycles of head decline and partial recovery since the 1940s in our study region. Specifically, we quantified the amount of subsidence in 2017 that was deferred from each cycle by fixing the head at the level observed at the end of the cycle and simulating the subsidence that would result, with no further changes in head, in 2017. The results, shown in Figure 2a, reveal that the deferred subsidence incrementally increased with each cycle. This cumulative effect is due to the long compaction timescales associated with the slow diffusion of head through thick clay interbeds and aquitards. For example, Figure 2b shows the 2017 head profile through a 13 m thick clay. The head levels in a 4 m thick zone in the center of the clay would still be greater than (so unequilibrated with) those in 1987, and for each cycle of head decline and recovery, the thickness of this zone increased. The cumulative effect of repeated cycles of head decline and partial recovery in a system governed by very long timescales has led to extremely high rates of deferred subsidence by 2017.

These high levels of deferred subsidence, ongoing today and previously unrecognized, represent a significant concern for groundwater managers for two main reasons. Firstly, they represent long-term subsidence rates which, in the absence of head recovery, will continue for decades into the future. Secondly, they are now established as the baseline so that any future head decline will add *additional* subsidence. Such high baseline rates mean the system is highly vulnerable to extremely large and damaging subsidence rates in the event of further head decline. This is of particular concern as the San Joaquin Valley enters another period of drought in Spring 2021. The high deferred subsidence rates in our study region are likely to be present widely across the Valley, where similar cycles of head decline and partial recovery have been observed for decades, and represent an acute challenge in the sustainable management of groundwater.

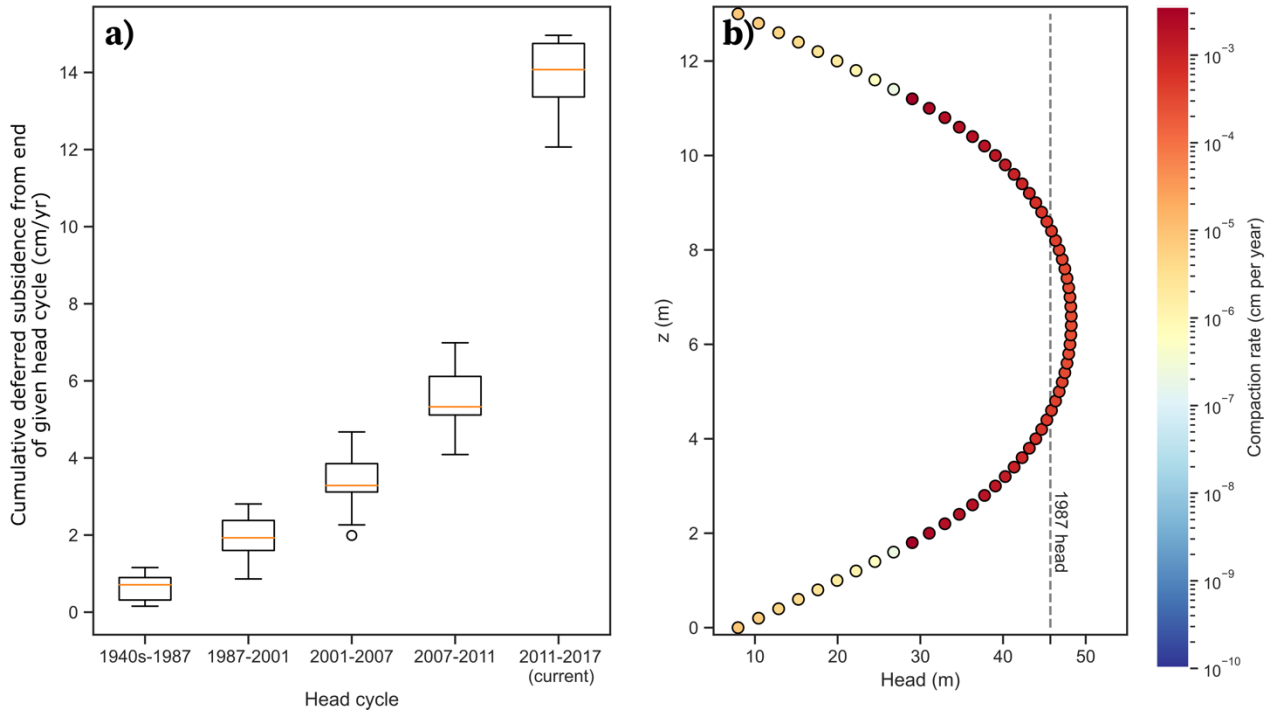


Figure 2 a) The cumulative deferred subsidence from the end of each head cycle. The box-and-whisker representation shows the range of rates simulated in the 27 model runs. b) A head-depth profile through a 13 m thick clay in 2017. Points are colored by their compaction rate. A compacting region approximately 4m thick in the core of the clay has head levels greater than 1987 levels. The illustrated clay comes from a simulation with characteristic timescale of compaction of 200 years.

Depth of compaction

The final important insight provided by our modeling approach is the depth at which compaction is occurring. Our model divided the aquifer system into the three major hydrostratigraphic layers: the unconfined to semi-confined upper aquifer, the Corcoran Clay and the confined lower aquifer, and we simulated the compaction in each. The apportionment of compaction between these three layers is shown in Figure 3. These data fill an important data gap left by the sparse extensometer network. Figure 3 is separated into two time periods, 1955-1980 and 2000-2017. In both periods, compaction of the Corcoran Clay contributed less than 10% of the total subsidence, and the majority of the subsidence occurred in the lower aquifer. This is consistent with the extensometer measurements from the Poland era as well as previous numerical experiments^{3,34,35}. However, an unexpected result was the relatively large amount of subsidence, up to 30%, which originated in the upper aquifer from 1955-1980. During this period, lower aquifer head levels were relatively constant whereas upper aquifer head levels showed a net decline. While it has often been assumed that subsidence is only a problem at locations where the Corcoran Clay is present, due to the confined conditions it creates in the underlying aquifer, our results show that under conditions of significant head decline, it is possible for substantial subsidence to originate within the unconfined-to-semi-confined upper aquifer. Our modelling approach could be generalized to other locations in the Valley, providing an alternative to the expense of installing extensometers and contributing critical information on the depth of compaction.

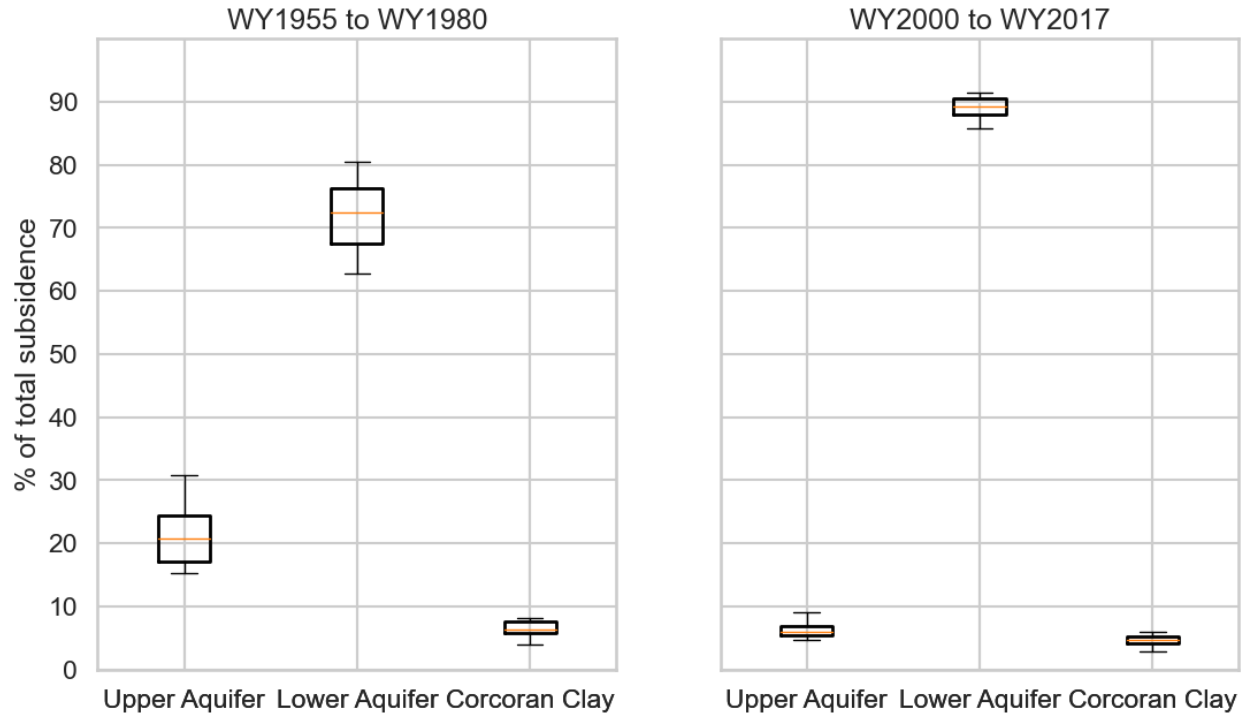


Figure 3 The portion of subsidence occurring from compaction in each hydrostratigraphic layer in 1955-1980 (left) and 2000-2017 (right). The box and whisker plots represent the range of results from the 27 model runs which fitted the validation data. The whiskers give the 5th and 95th percentiles, while the boxes cover the interquartile range. The orange bars show the median simulated values.

Conclusions

The sustainable management of groundwater can be guided by insights gained from observations of the past. We have used a one-dimensional numerical compaction model to obtain a 65-year record of head and simulated subsidence from 1952-2017 in a study region in the San Joaquin Valley. Our model provides insights into the long timescales over which subsidence occurs and highlights the presence of extremely high deferred subsidence rates. While we saw that the lower aquifer was the main source of subsidence, our model was able to highlight the capacity for both aquifers to contribute subsidence under conditions of sustained head decline. As the San Joaquin Valley enters another period of drought, and groundwater managers begin implementing their SGMA plans, our findings provide the critical quantitative insight into the causes of subsidence required to inform the sustainable management of groundwater.

Methods

Methods 1: Preparation of head inputs

In the San Joaquin Valley, it is generally difficult to construct long-term head time series corresponding to the upper and lower aquifers. The primary challenges are that well completion reports are seldom available, wells are often screened across both aquifers, and measurements are often either privately owned or contain unmarked errors³⁶. We had access to a large amount of groundwater data and were therefore able to resolve these challenges in our study region. The available datasets were: the statewide well data from the California Statewide Groundwater Elevation Monitoring (CASGEM) database³⁷; a complementary local database of water level measurements in the Kaweah groundwater subbasin, compiled by GSI Water Solutions and provided with the permission of several local groundwater agencies; water-level measurements from Poland et al. (1975)⁹; and water-level data from a dedicated monitoring well Well H, situated 2 km northeast of our study region, which had 4-hourly measurements of head in the upper and lower aquifers for the period 2015-present and were provided by Kings County Water District.

We categorized wells in our study region into four classes: gold standard upper aquifer wells, gold standard lower aquifer wells, supplementary upper aquifer wells and supplementary lower aquifer wells. Gold standard wells were those for which we had very high confidence of which aquifer the head measurements represented. To that end, gold standard upper aquifer wells were defined as those with available well completion information, well depth shallower than the Corcoran Clay, and seasonal amplitude variations similar to upper aquifer variations at Well H. Gold standard lower aquifer wells were those with well completion information available, perforated intervals exclusively below the Corcoran Clay, and seasonal amplitude variations similar to those in the lower aquifer at Well H. Corcoran Clay depths were determined from the borehole data as described in *Methods 3*. The two gold standard upper aquifer and two gold standard lower aquifer wells which we identified in our study region are highlighted in Table S 1. Unfortunately, using only these four wells would have left a head timeseries with gaps in the upper aquifer between 1978-2010 and gaps in the lower aquifer between 1981-2006. We identified supplementary wells to fill these gaps. Supplementary wells were additional wells which did not have completion information available but satisfied other criteria to give us confidence of the aquifer which they were recording. Supplementary wells were defined as those with head measurements which showed overlap with those from gold standard wells, and which showed seasonal variability similar to the corresponding aquifer at Well H. We identified two supplementary wells in each aquifer which, when combined with the gold standard wells, gave a continuous record of measurements from 1952-2017, shown in Figure S 4. The locations of five of the wells used are shown in Figure S 1. Since some of the measurements from the local head dataset are not publicly available, the exact locations of three of the wells are not shown.

To convert the well head measurements into model input for each aquifer, we extracted a Fall minimum and Spring maximum for each year, then linearly interpolated between those measurements. We excluded Well UA2 from this process due to anomalously low head measurements in 2007-10, and likewise removed two measurements taken in 1995 and 1976 from UA3 which were also anomalously low (Figure S 4). For each year, we defined the Fall

minimum as the minimum datapoint between the months of August and November (inclusive), and we defined the Spring maximum as the maximum datapoint between the months of January and May (inclusive); in the extremely rare case that no data were available within Spring or Fall, we used the measurement from the previous year (for instance, Upper Aquifer Fall 1977 and Fall 1976 are identical for this reason). We tested the validity of this approach by applying it to the continuously monitored data at Well H, and comparing subsidence simulated using our approach as input to that simulated using the “true”, continuously-recorded measurement as input. The differences, which can be seen in Figure S 5, were relatively minor.

The final head timeseries used as model input are presented in Figure S 6.

Methods 2: Model equations and numerical solver

The conceptual model of the subsurface, which forms the basis for our numerical model, is shown in Figure S 3. Our numerical implementation of the aquitard-drainage model follows that of Helm (1975)³⁸, and is summarized only briefly here. Clays appear in our model in three places: upper aquifer interbeds, lower aquifer interbeds and the Corcoran Clay aquitard. Within each clay layer, we solve the governing equation for effective stress:

$$\frac{K_v}{S_s} \frac{\partial^2 \sigma'}{\partial z^2} = \frac{\partial \sigma'}{\partial t} \quad \text{Equation M 1}$$

where σ' is the effective stress, K_v is the vertical hydraulic conductivity and S_s is the specific storage, related to skeletal specific storage S_{sk} by the relation $S_s = S_{sk} + S_{sw}$, where S_{sw} is the specific storage due to the compressibility of water. A detailed explanation of the concepts of specific storage can be found in p. 4-5 of Sneed (2001)³⁹. Equation M1 is solved using a finite difference scheme; our model code is available here:

https://github.com/mlees0209/compaction_model_StaticPaperVersion. The initial conditions for each clay layer are discussed in *Methods 5*. The effective stresses of the two aquifers, which act as boundary conditions and drive the system’s dynamics, are time-varying and are computed from the observed head in the aquifer layers using the relation $d\sigma' = d\sigma + \rho g dh$, in which σ is the overburden stress, ρ is the density of water and g is the gravitational acceleration.

Overburden stress is calculated based on the upper aquifer head according to $d\sigma = \rho g dh_{upper} S_y$ where S_y is the specific yield; this relationship is concisely explained in p. 5-6 of Poland et al. (1972)⁴⁰. For the interbeds, the boundary conditions are symmetric on the upper and lower boundaries. For the Corcoran Clay, the upper and lower boundary conditions are different, and are the effective stress in the upper and lower aquifers respectively.

An important part of Equation M1 is the hysteretic behavior of S_{sk} , which takes the following values depending on effective stress conditions at a given node (see p.5 of Sneed (2001)³⁹):

$$S_{sk} = \begin{cases} S_{ske} & \text{if } \sigma' < \max(\sigma') \\ S_{skv} & \text{if } \sigma' \geq \max(\sigma') \end{cases} \quad \text{Equation M 2}$$

To apply Equation M2, our model keeps track of effective stress history for each node and updates the value of S_{sk} accordingly.

Calculation of compaction for each clay layer follows Equation 8 in Helm (1975)³⁸, which is reproduced here, modified slightly to match our notation:

$$b(t_i) = \frac{\Delta z}{\rho g} \left[S_{skv} \sum_{j=1}^{J-1} (\max_{n \leq i}(\sigma_j^n) - \sigma_j^0) - S_{ske} \sum_{j=1}^{J-1} (\max_{n \leq i}(\sigma_j^n) - \sigma_j^i) \right] \quad \text{Equation M 3}$$

where $b(t_i)$ refers to the total compaction of the clay at timestep i , Δz is the mesh spacing, and there are J nodes. The nodes used are the midpoints of the nodes used to solve Equation M1; values of effective stress at the midpoints are obtained through linear interpolation. Superscripts on effective stress refer to the value at a given timestep. Note that, in the condition that effective stress at the current timestep is equal to its maximum, the S_{ske} term equates to zero and compaction is calculated purely as the inelastic sum.

In the coarse-dominated units, effective stress history was calculated as described previously. Compaction in these units was calculated using Equation 3 with $S_{skv} = 0$, an elastic value of S_{ske} for coarse-dominated material and a single ‘node’ of thickness Δz equal to the aquifer layer thickness minus the total thickness of clay interbeds within the aquifer.

The values used for all hydrologic parameters are provided in see *Methods 6*. The hydrostratigraphy of the subsurface is described in *Methods 3* and *4*.

Methods 3: Estimating the number and thickness of subsurface clays and the top and bottom boundaries of the Corcoran Clay

Borehole data, in the form of a driller’s log and a resistivity log, were both obtained at Well 19S22E08D002M. These logs were provided to us by Kaweah Delta Water Conservation District. The borehole was 210 m deep and both logs spanned its entire depth. The driller’s log contained generalized lithologic descriptions of the subsurface at 5-foot intervals but did not describe individual clay interbeds; an illustrative extract from the driller’s log is shown in panel a) of Figure S 7. The resistivity log was a 16-inch normal log which we interpreted presuming that clays are the least resistive layers.

To obtain the number and thickness of subsurface clays and the boundaries at the top and bottom of the Corcoran Clay, we applied resistivity cutoffs to the resistivity log. These resistivity cutoffs were values below which we assumed material to be clay. To choose appropriate cutoff values, we applied trial cutoffs and compared the result with our identification of the Corcoran Clay and thicker clay lenses from the driller’s log. We determined that the smallest and largest cutoffs which gave good agreement were 30.5 and 38.5 ohm-m respectively, shown in Figure S 7 panels b) and c). There was no variation in the depths to top or bottom of the Corcoran Clay across this range, which were 108 m and 135 m respectively. However, there was variation in the number and thickness of clay interbeds in each aquifer. We retained these variations in our grid search, and included two intermediate cutoffs of 33 and 36 ohm-m. The four resulting clay distributions are shown in Figure S 7 panels d-g. One complication was that, for most simulations, the lower

aquifer extended below the base of Well 19S22E08D002M (see *Methods 4* for our approach to estimating the aquifer system base). In these cases, on the basis that there is no evidence for a change in depositional environment below the log, we scaled the number of clays from within the log to correspond to the lower aquifer thickness. For instance, the log covered a 50 m thick region of the lower aquifer; in a simulation with a lower aquifer thickness of 100 m, we doubled the number of clay interbeds identified in the log.

Methods 4: Assigning depth to aquifer system base and defining top of upper aquifer

We defined the lower aquifer as the region below the Corcoran Clay over which significant head changes occurred. Although the deepest pumping well in our study region is 322 m deep, we expect head changes to propagate for some depth below this. This propagation depth will depend on the hydraulic conductivity of the lower aquifer and the time scale being considered. From resistivity logs, an impermeable layer called the San Joaquin Formation has been identified in our study region at about 800 m below the surface (see, for instance, Figure 14b in the Mid Kings River GSA³²), which we consider to be the maximum possible depth to which head changes propagate. However, to accurately determine the propagation of head changes in the region between the base of wells (322 m) and the base of permeable units (800 m), we would require a detailed hydrogeologic model in a region for which we have neither head measurements for validation nor well data to describe the subsurface structure. Instead, we made the simple approximation that head changes in the lower aquifer propagated for some depth-of-influence d_i below the deepest pumping well, as annotated in Figure S 3. Since we could not reliably know d_i , we allowed it to be a variable in our grid search. The base of the lower aquifer in our model was therefore defined as $z_{\text{base}} = z_{\text{deepestwell}} + d_i$. Unlike in the previous hydromechanical modelling studies of Helm (1975)³⁸ and Smith and Knight (2019)²³, this approach gave us a temporally-varying base of the lower aquifer, since $z_{\text{deepestwell}}$ has increased as more wells were drilled over time, as shown in Figure S 8. Data on the depths of wells drilled over time came from the California Department for Water Resources' Online System for Well Completion Reports (OSWCR), and is available at: <https://data.cnra.ca.gov/dataset/well-completion-reports>.

In our grid search, we let d_i take the values [50, 100, 150, 200] m. This gave a maximum base of the lower aquifer as 522 m, which is similar to the range used by Smith and Knight (2019)²³.

We defined the upper aquifer as the permanently saturated region throughout our modelled time period. We therefore defined the top of the upper aquifer to be the upper aquifer head in 2017, which was the lowest head during our modelled period, and was 41 m depth. This is illustrated in Figure S 3.

Methods 5: Assigning initial hydraulic head in clay layers

The initial hydraulic head condition within clays interbeds and aquitards cannot be measured, but it can be estimated based on the prior history of head in the aquifers³⁸. Given that the Poland-era record reveals that subsidence rates only became large at our study region in 1953⁹, we assumed that the initial head profile in the clay interbeds (h_0^{upper} and h_0^{lower}) were constant within each

aquifer. To select the values for h_0^{upper} and h_0^{lower} we considered what was known about head levels pre-1952.

In the upper aquifer, we identified CASGEM well 33014 within the study region which contained head data from 1925-1963. This well showed head approximately constant at a value of 68 masl from 1925-1948. From 1948, it dropped steadily to the model start value in 1952 (55 masl). We therefore bounded h_0^{upper} between 55 masl and 68 masl. For our grid search, we allowed values of 55, 61 and 68 masl.

In the lower aquifer, we were unable to identify any wells providing head information prior to 1952. Instead, we used the literature to give us a picture, albeit limited, of lower aquifer head levels. Mendenhall (1916)⁴¹ documented artesian wells tapping the deep aquifer in the study region in 1905; hence we know that lower aquifer head was at least the level of the land surface, or 71 masl, in 1905. By 1925, Harding (1927)⁴² reported that artesian wells in the valley had stopped flowing apart from in very wet winters. We do not, however, have any constraint on the deep aquifer head between 1925 and 1952. We therefore bounded h_0^{lower} as being between the 1952 level (39 masl) and the land surface (71 masl). For our grid search, we allowed values of 39, 49, 54, 60, 65 and 71 masl.

For the Corcoran Clay aquitard, we set the initial head h_0^{C-clay} to be constant, and equal to the average of the head in the upper and lower aquifers.

Methods 6: Selection of input hydrologic parameters

In the model equations described in *Methods 2*, there are seven hydrologic parameters: vertical hydraulic conductivity of clays K_v , elastic skeletal specific storage of clays and of coarse-dominated material (denoted here as S_{ske}^{cl} and S_{ske}^{co} respectively), inelastic skeletal specific storage of clays S_{skv} , the specific storage due to the compressibility of water S_{sw} , the density of water ρ and the acceleration due to gravity g . Three of these (S_{sw} , ρ and g) are well-known physical constants so did not vary in our grid search. Additionally, since $S_{ske}^{cl} \ll S_{skv}$ and $S_{ske}^{co} \ll S_{skv}$, we did not expect S_{ske}^{cl} or S_{ske}^{co} to have significant influence on our simulated subsidence, and we therefore did not vary them in our grid search. The values used for these five, non-varying parameters are given in the top part of Table S 2.

The remaining two variables (K_v and S_{skv}) were important to our simulations and we varied them in our grid search. Our approach was to define the range of values reported in the literature and run simulations which covered a large portion of that range. We gave extra weighting to values from previous models, as opposed to values from laboratory experiments, as it is known that values do not agree at these two scales³⁹. The literature ranges and the values used in our simulations are given in the bottom part of Table S 2.

Methods 7: Validation of model outputs

The four validation datasets, and the validation criteria, are described below.

2015-17 InSAR data

The 2015-17 InSAR data were acquired with the European Space Agency Sentinel satellite and processed by TRE Altamira under contract with the California Department of Water Resources (DWR), who provided them to us. A detailed description of how the data were processed can be found in TRE ALTAMIRA Inc. (2020)⁴³, and a version of the data is publicly available through the DWR website: <https://data.cnra.ca.gov/dataset/tre-altamira-insar-subsidence>. The raw data provided measurements of vertical displacement every 7-14 days, starting in February 2015 and continuing until the end of our study period, at the pixel locations seen in Figure S 9a and b. Since our model input head was based on a Fall minimum and a Spring maximum for each year (i.e., temporal resolution of six months), we degraded the temporal resolution of the validation data from 7-14 days to annual by using October-to-October values. This allowed us to validate our simulated subsidence over two water years: Water Year 2016 and Water Year 2017. The validation criteria for these two years were:

- 1) **Water Year 2016:** simulated subsidence between 20 and 34 cm, which was the range of measured subsidence at the pixels in our study region (Figure S 9a).
- 2) **Water Year 2017:** simulated subsidence between 9 and 15 cm, which was the range of measured subsidence at the pixels in our study region (Figure S 9b).

2007-10 InSAR data

The 2007-10 InSAR data were the ALOS data described in Smith and Knight (2019)²³. Although the raw ALOS data contained 15 measurements from between June 1st 2007 and July 2nd 2010, we elected to use the mean rate of subsidence over that period for our validation because this gave a more reliable estimate of the actual subsidence than the individual measurements, which likely contained some noise. The validation criteria rate between these dates was a mean subsidence rate between 7.0 and 16 cm/yr, which was the range of measured subsidence in our study region. (This range is shown visually in Figure S 9c.)

Highway 198 survey point

The Highway 198 survey point provided a single measure of the total subsidence between “the 1960s” and 2004 as 1.7m, as reported in Sneed et al. (2018)⁴⁴. Considering that “the 1960s” could refer to anytime between 1960 and 1969, we converted 1.7 m into a range of deformation rates from 3.9-5.0 cm/yr, equivalent to 1.7 m over 44 or 34 years. The survey point is just north of our study area, as shown in Figure S 1. At the survey point, measurements from the two InSAR datasets record subsidence rates at 75% of the rates within our region. To account for the fact that our study area likely experienced slightly higher subsidence rates than the measurements at this survey point, we extended the bound slightly, and therefore applied the following validation criteria: the simulated subsidence between 1965 and 2004 was required to be between 90% and 160% of that recorded by the Highway 198 survey point; that is, it had to have a mean rate over that period between 3.9 and 6.9 cm/yr.

Poland-era survey data

The Poland-era survey data are a series of measurements made during the years 1933, 1947, 1953/4, 1957, 1958, 1962, 1966 and 1970 as reported in Poland et al. (1975)⁹ and the Inter-Agency Committee on Land Subsidence in the San Joaquin Valley (1958)¹⁶. They show low rates of subsidence until 1953/4, and high rates of subsidence from then until the end of the surveyed period in 1970. Since the early part of our simulations is more strongly influenced by the initial conditions, we only used the 1966-1970 measurement as model validation. The survey

recorded an average subsidence rate of 11 cm/yr during those four years. However, the survey location is slightly south of our study region (see location in Figure S 1). At the survey location, measurements from the two InSAR datasets recorded subsidence rates 125% of the rates measured within our region. To account for the fact that our study area likely experienced slightly lower subsidence rates than the measurements at this survey point, we extended this bound slightly, and applied the following validation criteria: the simulated subsidence rate between 1966 and 1970 was required to be between 65% and 100% of that recorded by the survey point; that is, it had to have a mean rate over that period between 7 and 11 cm/yr.

Methods 8: Calculating characteristic time constant of compaction for a simulation

To calculate the characteristic time constant of compaction for a simulation, we applied equation 3 of Hoffman et al. (2003)⁴⁵, reproduced below:

$$\tau = \frac{b_{eq}^2 S_{skv}}{4K_v} \quad \text{Equation M 4}$$

where we use the values of S_{skv} and K_v for that particular simulation. To calculate the equivalent thickness b_{eq} , we follow the approach of Helm (1975)³⁸, using a version of their equation 9, modified to fit our notation:

$$b_{eq} = \sqrt{\frac{1}{\sum_i n_i} \sum_i n_i t_i^2} \quad \text{Equation M 5}$$

where there are i unique interbed thicknesses t_i in each model, and n_i is the number of each thickness. To be consistent with the results of Helm (1978)²⁵, we do not include the Corcoran Clay in this calculation, hence only consider interbeds; the time constants including the Corcoran Clay would be slightly larger.

References

1. Herrera-García, G. *et al.* Mapping the global threat of land subsidence. *Science* **371**, 34–36 (2021).
2. Bagheri-Gavkosh, M. *et al.* Land subsidence: A global challenge. *Science of The Total Environment* **778**, 146193 (2021).
3. Ireland, R. L., Poland, J. F. & Riley, F. S. *Land subsidence in the San Joaquin Valley, California, as of 1980*. <http://pubs.er.usgs.gov/publication/ofr82370> (1984).
4. Mastin, T., Styles, S. & Feist, K. A Review of Subsidence Measurements near Mendota, California. in *World Environmental and Water Resources Congress 2018* 50–61 (American Society of Civil Engineers, 2018). doi:10.1061/9780784481400.005.
5. Faunt, Sneed, M., Traum, J. & Brandt, J. T. Water availability and land subsidence in the Central Valley, California, USA. *Hydrogeol J* **24**, 675–684 (2016).
6. California Department of Water Resources. *California Aqueduct Subsidence Study: Supplemental Report*. 219 https://water.ca.gov/-/media/DWR-Website/Web-Pages/Programs/Engineering-And-Construction/Files/Subsidence/CASS_Supplement_final_a_1119.pdf (2019).
7. Feds release environmental review for Friant-Kern Canal project. *The Business Journal* <https://thebusinessjournal.com/feds-release-environmental-review-for-friant-kern-canal-project/> (2020).
8. Governor Newsom Expands Drought Emergency to Klamath River, Sacramento-San Joaquin Delta and Tulare Lake Watershed Counties. *California Governor* <https://www.gov.ca.gov/2021/05/10/governor-newsom-expands-drought-emergency-to-klamath-river-sacramento-san-joaquin-delta-and-tulare-lake-watershed-counties/> (2021).

9. Poland, J. F., Lofgren, B. E., Ireland, R. L. & Pugh, R. G. *Land Subsidence in the San Joaquin Valley, California, As of 1972*. 87 (1975).
10. *Land subsidence in the United States*. (U.S. Geological Survey, 1999).
11. Ingerson, I. M. The hydrology of the Southern San Joaquin Valley, California, and its relation to imported water-supplies. *Eos, Transactions American Geophysical Union* **22**, 20–45 (1941).
12. *Guidebook to studies of land subsidence due to ground-water withdrawal*. (United Nations Educational, Scientific and Cultural Organization (UNESCO), 1984).
13. Shirzaei, M. *et al.* Measuring, modelling and projecting coastal land subsidence. *Nature Reviews Earth & Environment* **2**, 40–58 (2021).
14. Ireland, R. Land Subsidence in the San Joaquin Valley, California, as of 1983. (1986).
15. Borchers, J. & Carpenter, M. Land Subsidence from Groundwater Use in California. (2014).
16. Inter-Agency Committee on Land Subsidence in the San Joaquin Valley. *Progress Report: Land-Subsidence Investigations San Joaquin Valley, California Through 1957*. (1958).
17. Swanson, A. Land Subsidence in the San Joaquin Valley, Updated to 1995. (1998).
18. Halverson, N. California is literally sinking into the ground. *Mother Jones* <https://www.motherjones.com/environment/2015/06/california-sinking-drought-ground-water/> (2015).
19. The Sun-Gazette. Feds approve \$5M to begin repairs on Friant-Kern Canal. *The Sun-Gazette Newspaper* <https://thesungazette.com/article/business/2020/11/11/feds-approve-5m-to-begin-repairs-on-friant-kern-canal/> (2020).
20. Farr, T. G. & Liu, Z. Monitoring Subsidence Associated with Groundwater Dynamics in the Central Valley of California Using Interferometric Radar. *Remote Sensing of the Terrestrial Water Cycle* **9781118872**, 397–406 (2014).
21. Farr, T. G., Jones, C. & Zhen, L. *Progress Report: Subsidence in the Central Valley, California*. <https://data.cnra.ca.gov/dataset/nasa-jpl-insar-subsidence/resource/17ad6fd5-918b-4cb2-b682-940ed1c8deb2> (2015).
22. Farr, T. G., Jones, C. E. & Liu, Z. *Progress Report: Subsidence in California, March 2015 – September 2016*. 37 <https://data.cnra.ca.gov/dataset/nasa-jpl-insar-subsidence/resource/5a030395-3919-4e3a-b7be-fc272ea544fb> (2016).
23. Smith & Knight. Modeling Land Subsidence Using InSAR and Airborne Electromagnetic Data. *Water Resources Research* **55**, 2801–2819 (2019).
24. Liu, Z. *et al.* Monitoring Groundwater Change in California’s Central Valley Using Sentinel-1 and GRACE Observations. *Geosciences* **9**, 436 (2019).
25. Helm, D. C. Field Verification of a One-Dimensional Mathematical Model for Transient Compaction and Expansion of a Confined Aquifer System. in 189–196 (ASCE, 1978).
26. Smith, R. G. *et al.* Estimating the permanent loss of groundwater storage in the southern San Joaquin Valley, California. *Water Resources Research* 5998–6017 (2017) doi:10.1002/2016WR019804.Received.
27. Ojha, C., Werth, S. & Shirzaei, M. Groundwater Loss and Aquifer System Compaction in San Joaquin Valley During 2012–2015 Drought. *Journal of Geophysical Research: Solid Earth* **124**, 3127–3143 (2019).
28. Holzer, T. The History of the Aquitard-Drainage Model. *Land Subsidence Case Studies and Current Research. Proceedings of the Dr. Joseph F. Poland Symposium on Land Subsidence* 7–12 (1998).
29. Bertoldi, G. L., Johnston, R. H. & Evenson, K. D. Ground water in the Central Valley, California; a summary report. *US Geological survey professional paper no. 1401-A*, 55–55 (1991).
30. Croft, M. G. & Gordon, G. V. *Geology, hydrology, and quality of water in the Hanford-Visalia area, San Joaquin Valley, California*. (1968).
31. Austin, J. T. *Floods and droughts in the Tulare Lake Basin*. (Sequoia Natural History Association, 2015).
32. Mid Kings River GSA. Tulare Lake Subbasin Groundwater Sustainability Plan, January 2020.

33. Ojha, C., Farr, T. G., Werth, S., Shirzaei, M. & Argus, D. F. Sustained Groundwater Loss in California's Central Valley Exacerbated by Intense Drought Periods. *Water Resources Research* **54**, 4449–4460 (2018).
34. Sneed, M., Brandt, J. & Solt, M. Integration of remotely-sensed and ground-based measurements to constrain simulations of groundwater flow and land subsidence, San Joaquin Valley, CA. *AGU Fall Meeting Abstracts* **43**, H43D-1248 (2011).
35. Sneed, M., Brandt, J. & Solt, M. *Land Subsidence along the Delta-Mendota Canal in the Northern Part of the San Joaquin Valley, California, 2003–10*. (2013).
36. Brewster, B. *et al.* California's Groundwater Update 2013 - Appendix "E" Calculating Annual Change in Groundwater Storage Using Groundwater Level Data Contents. 1–23 (2015).
37. California Department of Water Resources. Periodic Groundwater Level Measurements. (2021).
38. Helm, D. C. One-dimensional simulation of aquifer system compaction near Pixley, California: 1. Constant parameters. *Water Resources Research* **11**, 465–478 (1975).
39. Sneed, M. *Hydraulic and Mechanical Properties Affecting Ground-Water Flow and Aquifer System Compaction, San Joaquin Valley, California*. (2001).
40. Poland, J. F., Lofgren, B. E. & Riley, F. S. Glossary of Selected Terms Useful in Studies of the Mechanics of Aquifer Systems and Land Subsidence due to Fluid Withdrawal. 14 (1972).
41. Mendenhall, W. C., Dole, R. B. & Stabler, H. *Ground water in San Joaquin Valley, California*. *Water Supply Paper* <https://pubs.er.usgs.gov/publication/wsp398> (1916) doi:10.3133/wsp398.
42. Harding, S. T. *Ground Water Resources of the Southern San Joaquin Valley*. (1927).
43. TRE ALTAMIRA Inc. *InSAR land surveying and mapping services in support of the DWR SGMA program - Technical Report March 2020*. <https://data.cnra.ca.gov/dataset/tre-altamira-insar-subsidence/resource/2535a9b9-ed25-4b19-9734-4b1409e3fdce> (2020).
44. Sneed, M., Brandt, J. T. & Solt, M. *Land Subsidence Along the California Aqueduct in West-Central San Joaquin Valley, California, 2003–10*. (2018).
45. Hoffmann, J., Galloway, D. & Zebker, H. A. Inverse modeling of interbed storage parameters using land subsidence observations, Antelope Valley, California. *Water Resources Research* **39**, (2003).
46. Faunt. *Groundwater Availability of the Central Valley Aquifer, California Introduction, Overview of Hydrogeology, and Textural Model of California's Central Valley*. (2009).
47. Leake, S. & Galloway, D. *MODFLOW ground-water mode: user guide to the Subsidence and Aquifer-System Compaction Package (SUB-WT) for water-table aquifers*. <https://pubs.usgs.gov/tm/2007/06A23/pdf/TM6a23.pdf> (2007).

Acknowledgements

We would like to thank Larry Dotson (Kaweah Delta Water Conservation District) for providing the borehole datasets and Dennis Mills (Kings County Water District) for providing the continuously-monitored head data at Well H. We thank Tim Nicely, Eric Osterling and Larry Dotson for providing the local head dataset. This work was funded by the Gordon and Betty Moore Foundation (grant no. GBMF6189) and by the NASA Applied Sciences Water Resources Program in the Earth Science Division (grant no. 80NSSC19K12480), with M. Lees supported by a Stanford Graduate Fellowship.

Data availability

The major datasets generated during and/or analyzed during the current study are available from the corresponding author on reasonable request. A small number of hydraulic head measurements belong to private groundwater agencies and due to the confidential nature of these data are not available on request. All head data are displayed in the paper in Figure S4.

Author Contributions

M.L and R.K designed the research. M.L performed the analysis with input from R.K and R.S. M.L drafted the manuscript and all authors participated in the manuscript editing.

Competing interests

The authors declare no competing interests.

Materials and Correspondence

Correspondence and requests for materials should be addressed to Matthew Lees at mlees0209@gmail.com.

Extended data

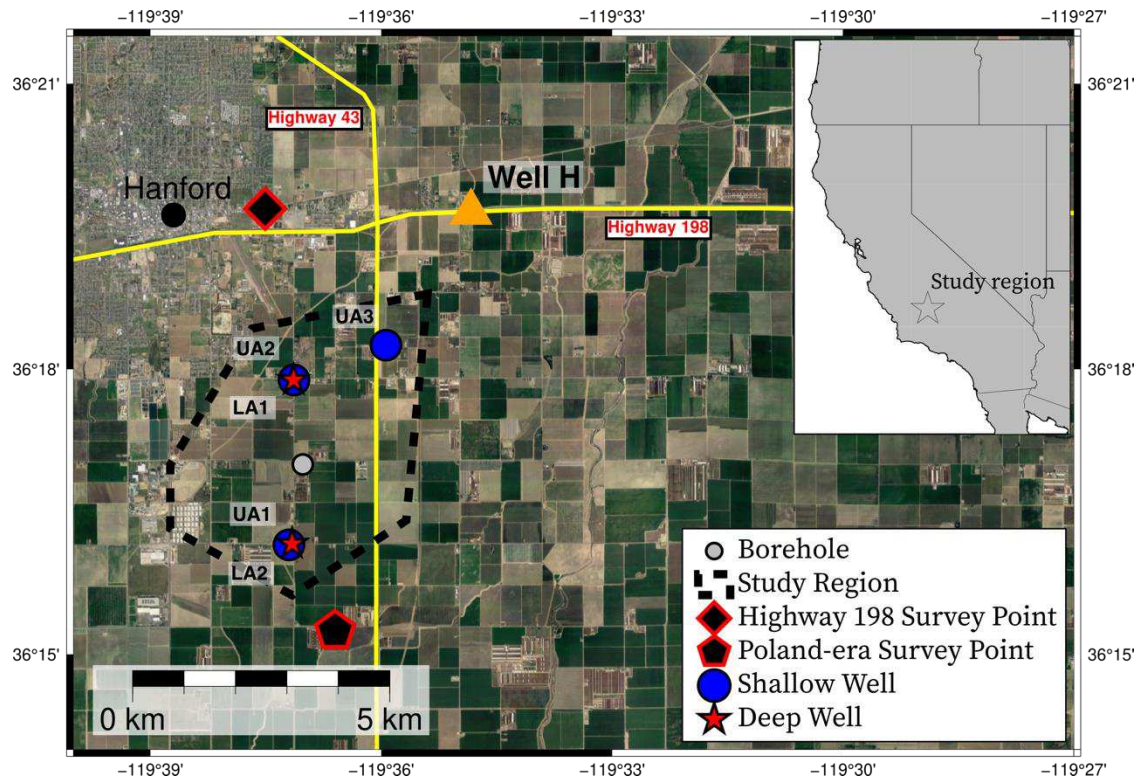


Figure S 1 Location map, showing the study region within California (inset). The main panel shows the study region in relation to the data used to populate the model, as well as the city of Hanford and major highways. Locations of Wells UA4, LA3 and LA4 are not shown as data from these wells are not publicly available. The locations of the Highway 198 levelling data and Poland-era levelling data used as model validation are also shown.

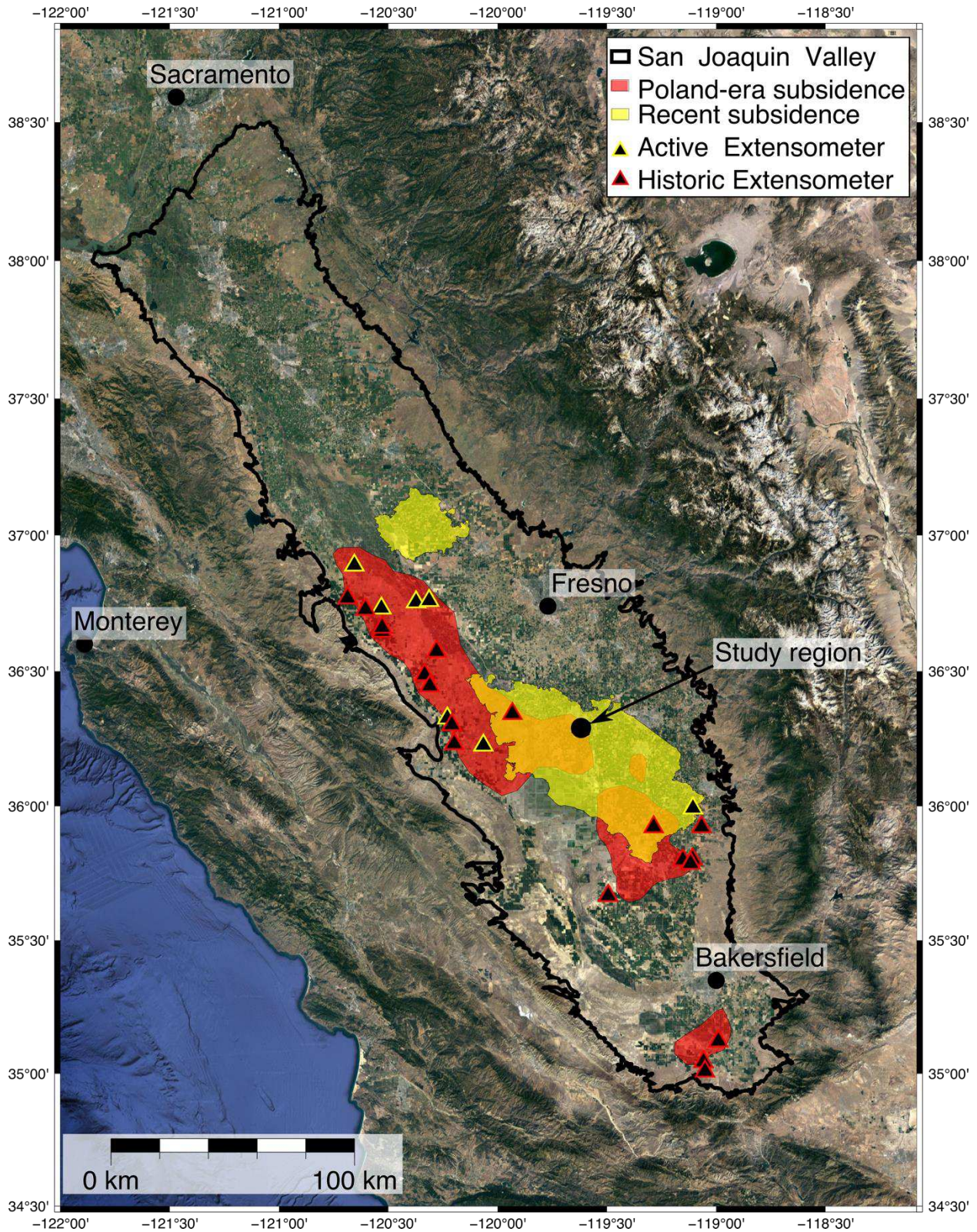


Figure S 2 Location of active and defunct extensometers in relation to recent and Poland-era land subsidence in the San Joaquin Valley. Poland-era subsidence is the 4-foot 1926-1970 subsidence contour, traced from Ireland et al (1984)³. The recent subsidence is the 10cm/yr contour for the period 2015-17, extracted from the TRE Altamira dataset; this dataset is described in Methods 7. Extensometer locations are gathered from the USGS's California Water Science Center

(https://ca.water.usgs.gov/land_subsidence/central-valley_extensometer-data.xlsx), from the dataset associated with Faunt et al. (2009)⁴⁶ (https://water.usgs.gov/GIS/metadata/usgswrd/XML/subsidence_measured_data.xml), and from Poland et al. (1975)⁹.

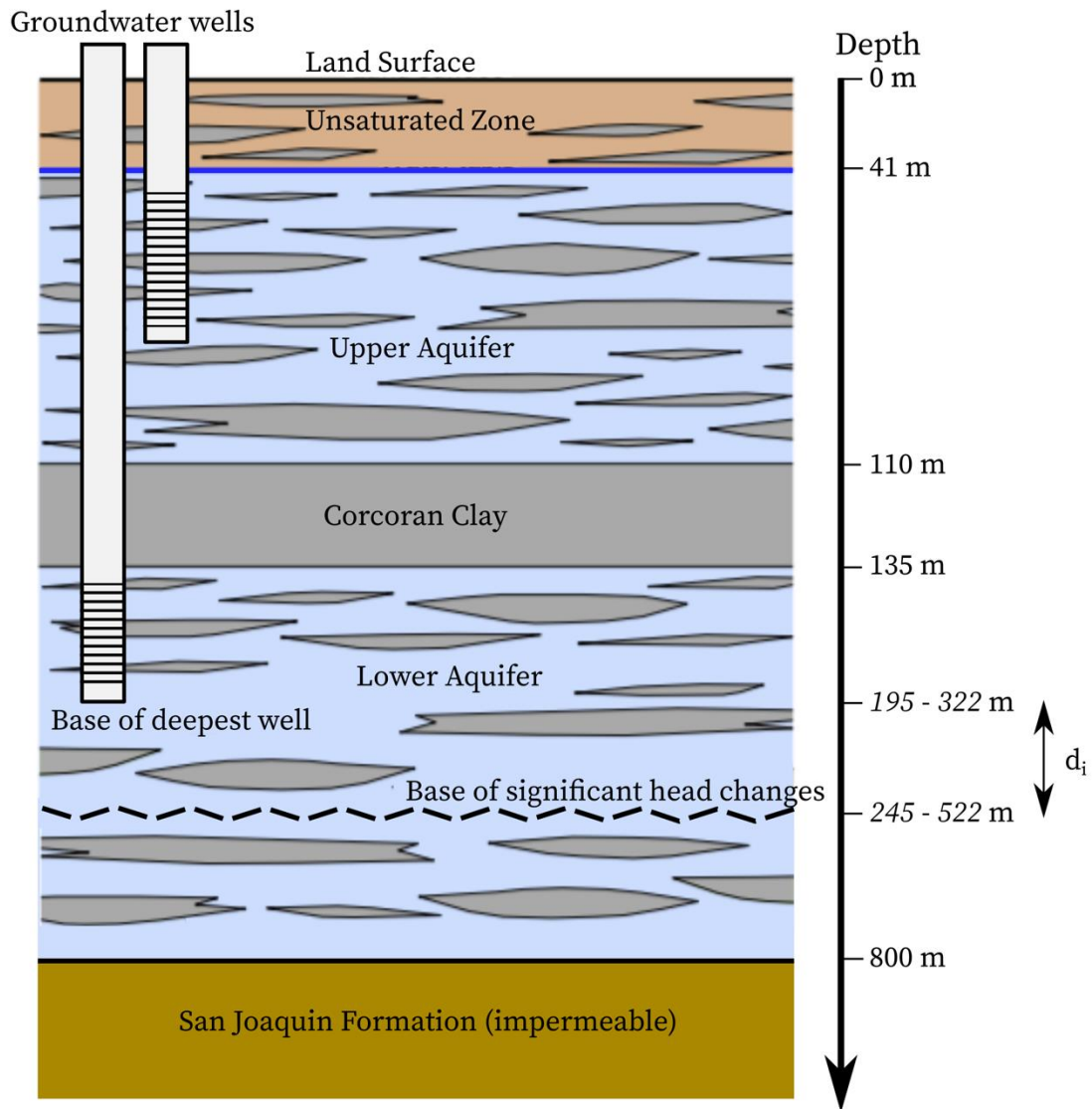


Figure S 3 Model hydrostratigraphy. *Italicized depths refer to depths which vary either with time (base of deepest well) or within the grid search (d_i).* Figure style adopted from Leake and Galloway (2007)⁴⁷.

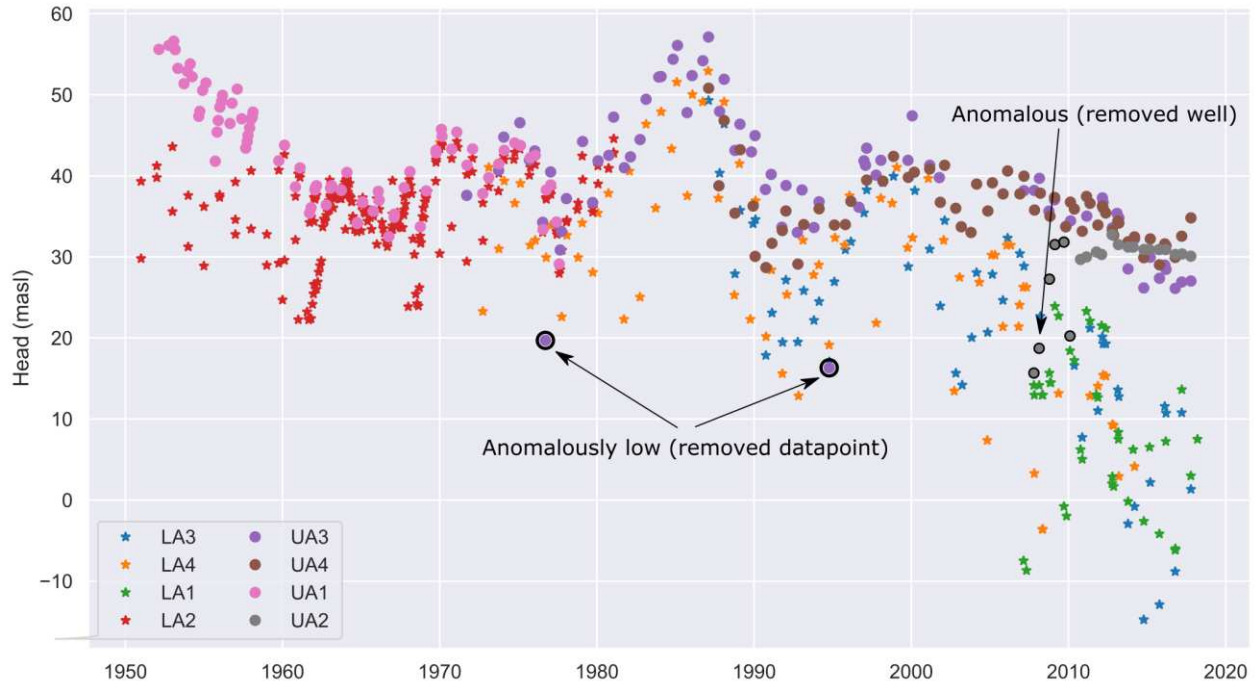


Figure S 4 All well data from the gold standard and supplementary wells. The anomalously low measurements which were removed are circled in thick black and are labelled, as are the anomalous measurements which led to the removal of Well UA2.

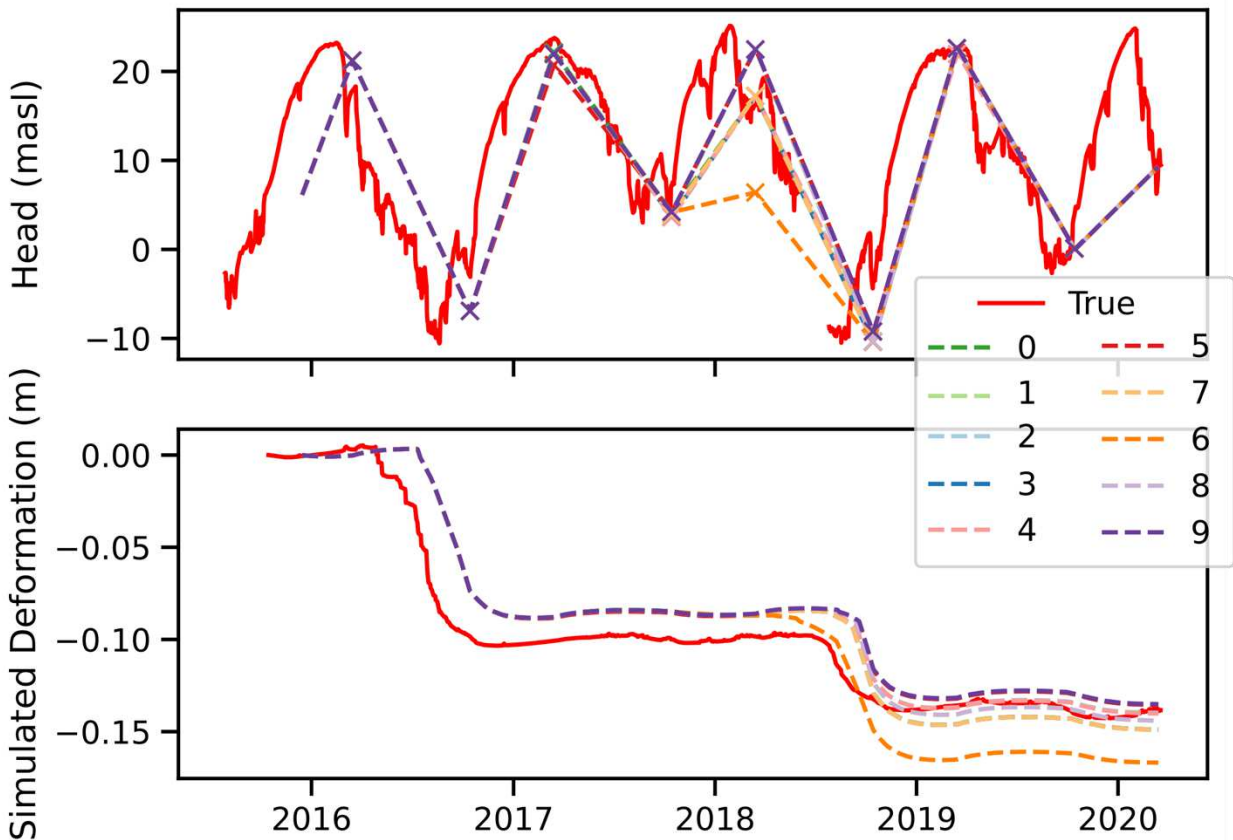


Figure S 5 Top: the true head timeseries, observed at Well H (solid red), and 10 reconstructed time series created using our interpolation approach (dashed lines). The 10 series were created using a head measurement from random months from the

Spring or Fall period of each year (Aug-Nov for Fall and Jan-May for Spring). Bottom: comparison between the simulated subsidence when using the true head timeseries (red solid line) and each of the 10 reconstructed time series (dashed lines). Our reconstruction approach leads to relatively minor differences in simulated subsidence when compared to using the true data.

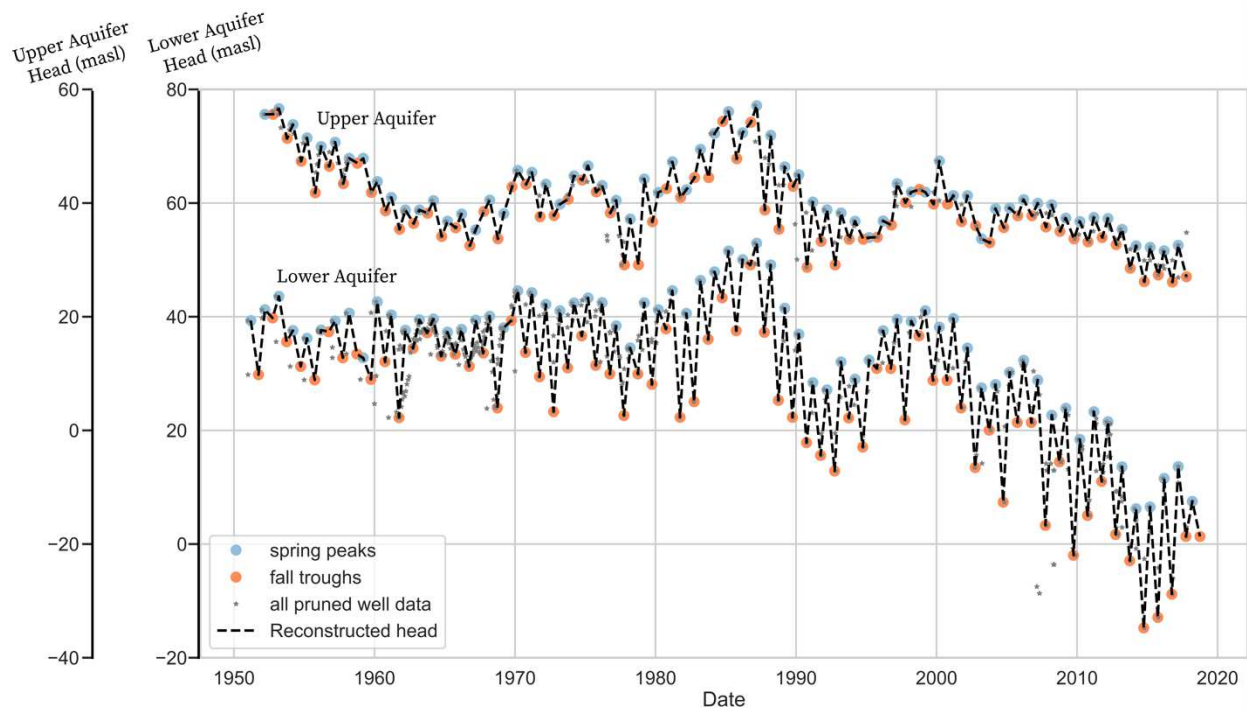


Figure S 6 The interpolated head data used as model input, plotted on top of the Spring Maxima, Fall Minima and raw data used to construct the input.

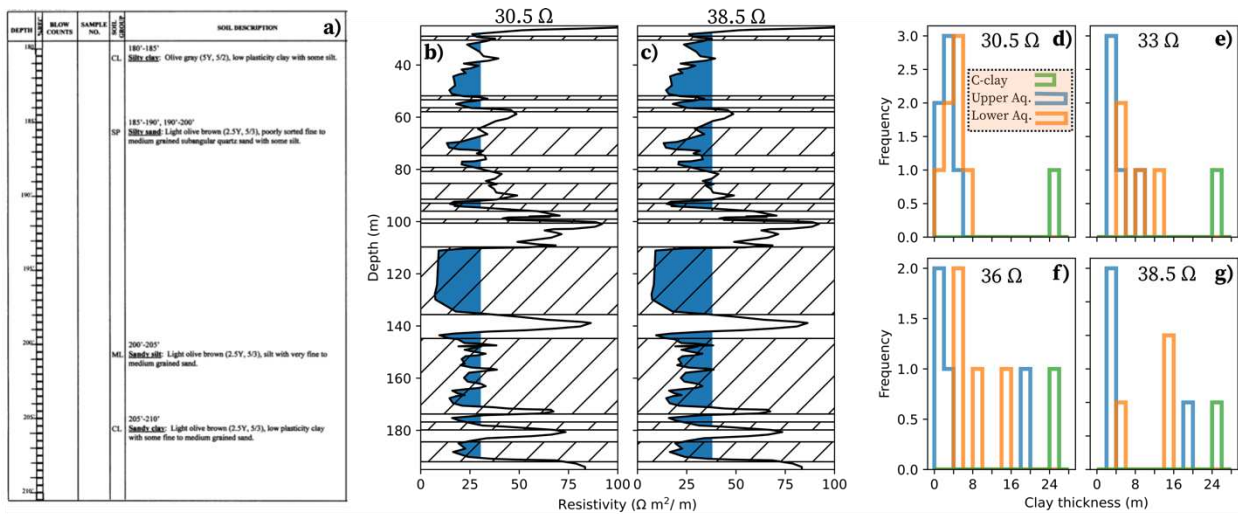


Figure S 7 a) Extract from the driller's log; b) and c) Two plots showing the resistivity log (black curve) and the clay layers deduced from the driller's log (hatched shading) for a resistivity threshold of 30.5 and 38.5 ohm-ms respectively. The region to the left of the threshold is shaded in blue. The Corcoran Clay is between 108 and 135 m depth. d-g) The four resulting versions of the clay distributions which were used in the grid search.

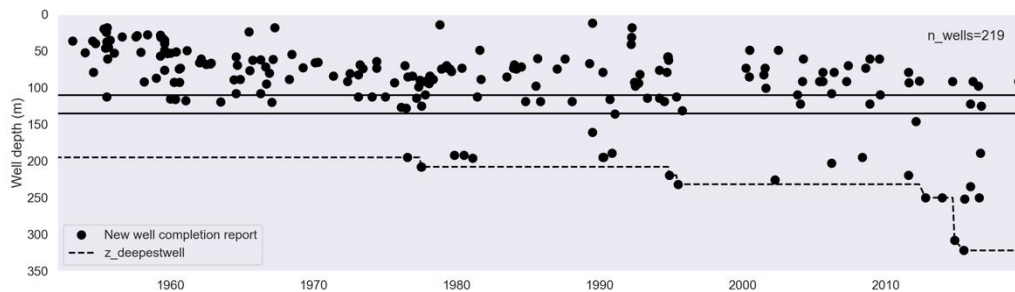


Figure S 8 Well completion records showing the drilling of new wells from 1952-2017 in our study region. The data were obtained from the OSWCR database. The two solid horizontal lines show the top and bottom of the Corcoran Clay at the borehole location. The dashed line is the time-varying trace of the depth to the deepest well. Note that, prior to 1969, it was not mandatory for completion reports of new wells to be submitted, so we have no data from 1952-1969. We expected that the depth to the deepest well in this period was similar to the 70s and 80s, and therefore have continued the dashed line backwards to 1952.

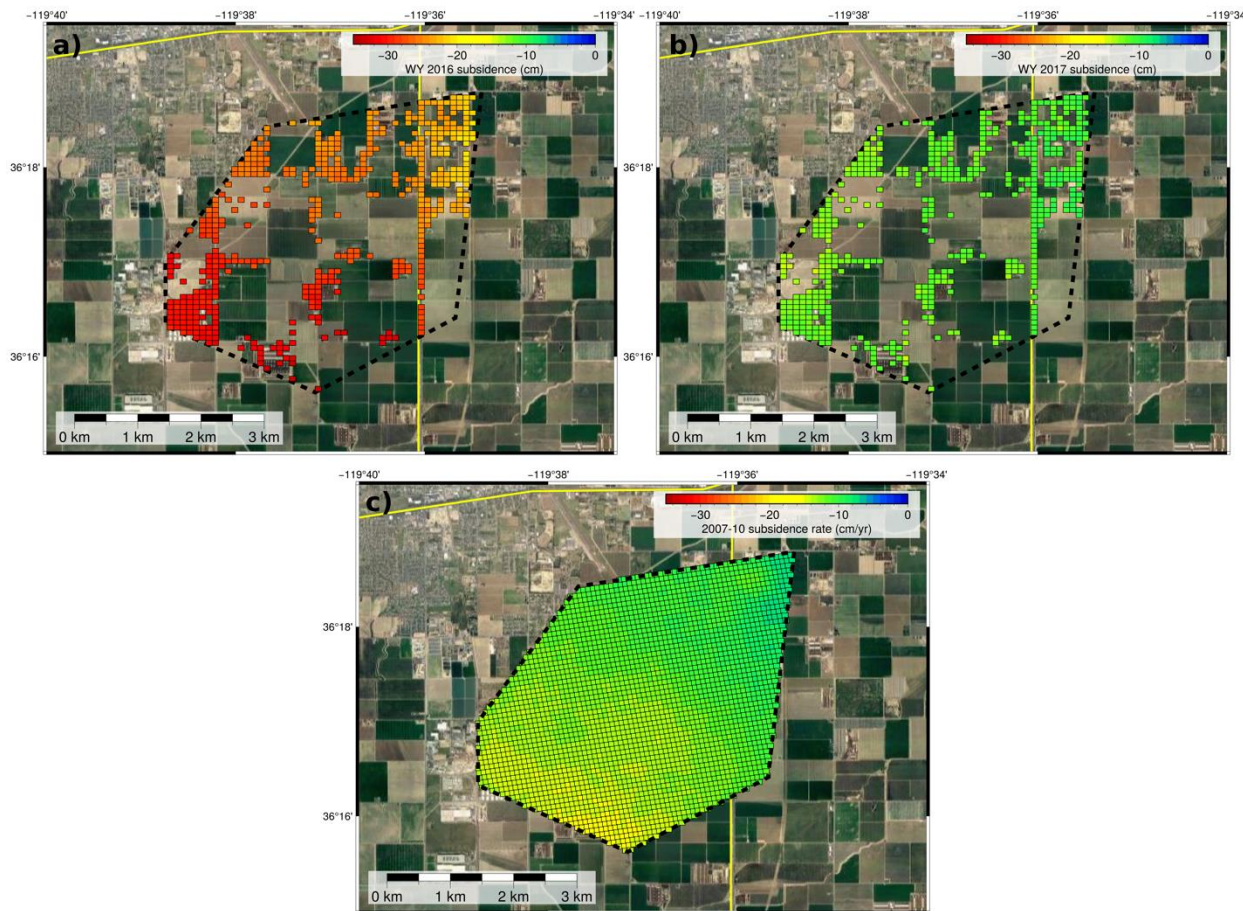


Figure S 9 a) The Water Year 2016 subsidence observed in our study region; b) the Water Year 2017 subsidence observed in our study region; c) the 2007-10 subsidence rate observed in our study region. In all three panels, the study region is shown as the black dashed outline, and InSAR pixels are shown individually; in panel c), the data were interpolated such that there is spatially continuous coverage.

Table S 1 Information on the wells used to create input head timeseries. Well name refers to the short name used for the purposes of this paper and, where possible, the California State Well number. For certain wells from the local head dataset, the California State Well number is not given because the head measurements are not publicly available. Gold standard wells have gold shading.

Well name(s)	Data Source(s)	Well depth (m)	Screened interval depth (m)	Period of coverage	Classification
Upper Aquifer Wells					
UA1 / 19S22E19A002M	CASGEM, Poland et al. (1975) ⁹	34 (taken from Poland et al. (1975) ⁹)	NA	1951-1978	Gold Standard Upper Aquifer Well
UA2 / 19S22E08D92M	Local head dataset	108	96-108	2010-present	Gold Standard Upper Aquifer Well
UA3 / 19S22E04M001M	CASGEM, Local head dataset	N/A	N/A	1971-2017	Supplementary Upper Aquifer Well
UA4	Local head dataset	N/A	N/A	1987-2017	Supplementary Upper Aquifer Well
Lower Aquifer Wells					
LA1 / 19S22E08D002M	Local head dataset and CASGEM	149	136-149	2006-2019	Gold Standard Lower Aquifer Well
LA2 / 19S22E19A001M	Poland et al. (1975) ⁹ and CASGEM	N/A	170 (taken from Poland et al. (1975) ⁹)	1952-1981	Gold Standard Lower Aquifer Well
LA3	Local head dataset	N/A	N/A	1987-2017	Supplementary Lower Aquifer Well
LA4	Local head dataset	N/A	N/A	1970-2013	Supplementary Lower Aquifer Well

Table S 2 The values used for all hydrologic parameters in the grid search. The top section of the table gives parameter values for the parameters which did not vary in the grid search; the bottom section gives the values of the parameters which did vary.

<i>Non-varying parameters</i>		
Parameter name	Value used in grid search	Source
S_{sw}	$1.5 \times 10^{-6} \text{ m}^{-1}$	Smith et al. (2017) ²⁶ p.3
ρ	1000 kg m^{-3}	N/A
g	9.81 ms^{-2}	N/A
S_{ske}^{cl}	$1.35 \times 10^{-5} \text{ m}^{-1}$	Faunt et al. (2009) ²⁷ Table C8
S_{ske}^{co}	$4.8 \times 10^{-6} \text{ m}^{-1}$	Faunt et al. (2009) ⁴⁶ Table C8
<i>Varying parameters</i>		
Parameter name	Literature range and source(s)	Values used in grid search
K_v	1.1e-6 to 1.4e-2 m day ⁻¹ from Faunt et al. (2009) ⁴⁶ and Smith and Knight (2019) ²³	[2.5e-7, 5e-7, 1e-6, 1.5e-6, 2e-6, 2.5e-6, 3e-6] m day ⁻¹
S_{skv}	4.6e-4 to 2.9e-3 m ⁻¹ from Faunt et al. (2009) ⁴⁶ and Smith and Knight (2019) ²³	[6e-4, 1.0e-3, 1.8e-3, 2.6e-3, 3.0e-3] m ⁻¹